How to cite: *Angew. Chem. Int. Ed.* **2024**, *63*, e202402344
doi.org/10.1002/anie.202402344

Structure Elucidation **Hot Paper**

Unusual Stabilisation of Remarkably Bent Tetra-Cationic Tetra-radical Intermolecular Fe(III) μ-Oxo Tetranuclear Complexes

Sabyasachi Sarkar, Rupesh Kumar Tiwari, Deepannita Samanta, Tapas Guchhait, E. Carolina Sañudo, Gopalan Rajaraman, and Sankar Prasad Rath**

Abstract: A hitherto unknown series of air stable, π-conjugated, remarkably bent tetra-cation tetra-radical intermolecular Fe(III) μ-oxo tetranuclear complex, isolated from the dication diradical diiron(III) porphyrin dimers, has been synthesised and spectroscopically characterised along with single crystal X-ray structure determination of two such molecules. These species facilitate long-range charge/radical delocalisation through the bridge across the entire tetranuclear unit manifesting an unusually intense NIR band. Assorted spin states of Fe(III) centres are stabilised within these unique tetranuclear frameworks: terminal six-coordinate iron centres stabilise the admixed intermediate spin states while the central five-coordinate iron centres stabilise the high-spin states. Variable temperature magnetic susceptibility measurements indicated strong antiferromagnetic coupling for the Fe(III)–O–Fe(III) unit while the exchange interactions between the Fe centres and the porphyrin π-cation radicals are weaker as supported both by magnetic data and DFT calculations. The nature of orbital overlap between the SOMOs of Fe(III) and π* orbital of the porphyrin was found to rationalise the observed exchange coupling, establishing such a complex magnetic exchange in this tetranuclear model with a significant bioinorganic relevance.

[*] Dr. S. Sarkar, D. Samanta, Dr. T. Guchhait, Prof. S. P. Rath
Department of Chemistry, Indian Institute of Technology Kanpur, Kanpur-208016, India
E-mail: sprath@iitk.ac.in

R. K. Tiwari, Prof. G. Rajaraman
Department of Chemistry, Indian Institute of Technology Bombay, Mumbai-400076, India
E-mail: rajaraman@chem.iitb.ac.in

Prof. E. C. Sañudo
Secció de Química Inorgànica, Department de Química Inorgànica i Orgànica, Facultat de Química, Universitat de Barcelona, C/Martí i Franqués 1–11, 08028 Barcelona, Spain

Prof. E. C. Sañudo
Institut de Nanociència i Nanotecnologia, IN2UB, Universitat de Barcelona, C/Martí i Franqués 1–11, 08028 Barcelona, Spain

Introduction

The vast family of multiheme proteins are the molecular machineries architectured by Nature to perform a wide range of enzymatic transformations that require multiple electrons coupled with long range electron transfer (ET).[1] The structural disposition of the heme units and the consequent intermacrocyclic interactions have been proposed to be highly significant in their various functions in such a widely distributed family.[1] To comprehend such intermacrocyclic interaction along with their relative orientations, the porphyrin units are linked covalently by different spacers to produce a large variety of porphyrin dimers.[2–7] The choice of such spacers allow us to precisely control the heme-heme interactions, their spatial orientation and also the possible electronic communication through the bridge. Due to such interactions, the di/multiheme cytochromes display significant differences in the structure and properties in comparison to the monohemes.[6,7] The small tetraheme cytochrome (STC), one of the widely available soluble ET proteins present in *Shewanella* during its growth in anaerobic conditions; the stereoview of the fully oxidised species has been shown in Figure 1A.[1e] The X-ray structure revealed that the hemes in STC are situated to form an elongated chain that spans ~23.06 Å between the two distant iron centres. Further investigation suggests a promiscuous "electron-harvesting" role for the protein in contrast to a classic predetermined electronic path along a "heme-wire".[1e]

Our recent studies focus on the radical-stabilising abilities of covalently linked porphyrin dimers with fully π-conjugated backbone.[8,9] In these systems, porphyrinoids involve the effective spin delocalisation throughout the π-conjugated framework and thereby enhancing the stability of the radicals. However, fabrication of a fully π-conjugated stable tetra-heme tetra-cation tetra-radical system bearing a μ-oxo motif, to the best of our knowledge, is the first of its kind. These are also the first X-ray structural reports of intermolecular diiron(III) μ-oxo tetranuclear complexes. Moreover, this unique class of molecule stabilises various spin states of Fe(III) within a single molecular framework: terminal porphyrinato cores stabilise the admixed intermediate spin states while the central porphyrinato cores stabilise the high spin states of Fe(III).

In the present study, starting from the dication diradical species of dichlorodiiron(III) porphyrin dimers **1**·$(X)_2$ (X=ClO_4^-, $CF_3SO_3^-$, $CH_3SO_3^-$ and BF_4^-), a series

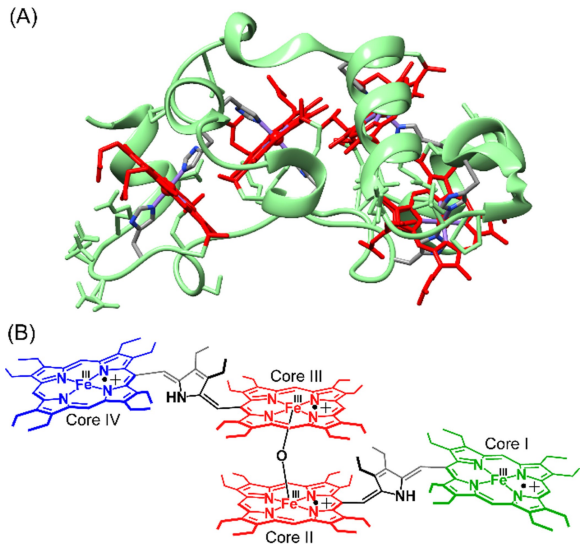

Figure 1. (A) Stereoview of small tetraheme cytochrome *c* (isolated from *Shewanella Oneidensis*) (PDB code 1M1R),[1e] the heme units and the protein chains are coloured red and green, respectively, and (B) tetra-heme unit reported here (axial coordination and counter anions are not shown).

of π-conjugated tetra-cationic tetra-radical intermolecular μ-oxo tetranuclear complex $\mathbf{2}\cdot(X)_6$ have been synthesised and spectroscopically characterised along with single crystal X-ray structure determination of two such molecules. These species facilitate long-range charge/radical delocalisation through the bridge across the tetranuclear unit and thereby display a highly intense near infrared (NIR) band (see below).

Results and Discussion

Synthesis

Dichlorodiiron(III) pyrrole-bridged dication diradical octaethylporphyrin dimers $\mathbf{1}\cdot(X)_2$ (X=ClO_4^-, $CF_3SO_3^-$, $CH_3SO_3^-$ and BF_4^-) have been synthesised upon oxidation of the corresponding dichlorodiiron(III) porphyrin dimer (**1**) using a reported procedure.[9] Starting from these dication diradical species $\mathbf{1}\cdot(X)_2$, a series of tetra-cation tetra-radical intermolecular μ-oxo tetranuclear complex $\mathbf{2}\cdot(X)_6$ was obtained just by adding trace amount of H_2O in nearly quantitative yields. Figure 2A shows the synthetic outline and the list of intermolecular μ-oxo tetranuclear complexes reported here. The complexes were then isolated as crystalline solid in good yields and subsequently characterised spectroscopically including structure determination of two such complexes, $\mathbf{2}\cdot(ClO_4)_6$ and $\mathbf{2}\cdot(BF_4)_6$. These tetra-radical complexes are air-stable

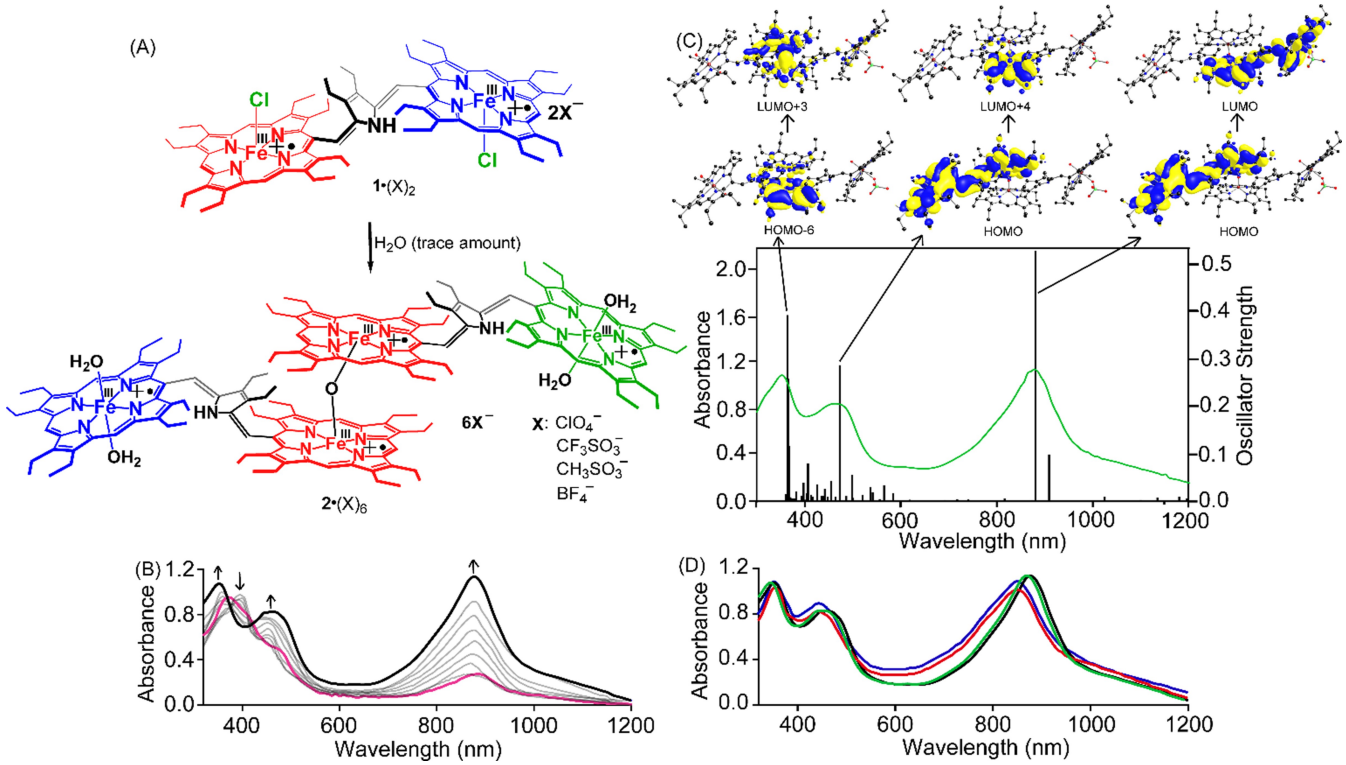

Figure 2. (A) Synthetic outline of the tetranuclear complexes along with the abbreviations used. (B) UV/Vis-NIR (in CH_2Cl_2 at 283 K) spectral changes of 0.5×10^{-5} M solution of $\mathbf{1}\cdot(ClO_4)_2$ after addition of trace amount of H_2O to form $\mathbf{2}\cdot(ClO_4)_6$. (C) UV/Vis-NIR spectrum (curved line, left axis) in CH_2Cl_2 and oscillator strengths (vertical line, right axis) obtained from TD-DFT calculations at the cam-B3LYP/6-31G**/LANL2DZ level of theory for $\mathbf{2}\cdot(ClO_4)_6$ and (D) UV/Vis-NIR spectra (in CH_2Cl_2 at 298 K) of 0.5×10^{-5} M solution of $\mathbf{2}\cdot(CF_3SO_3)_6$ (red trace), $\mathbf{2}\cdot(CH_3SO_3)_6$ (blue trace), $\mathbf{2}\cdot(ClO_4)_6$ (black trace) and $\mathbf{2}\cdot(BF_4)_6$ (green trace).

and can be stored in the solid state for a long period under ambient condition.

UV/Vis-NIR Spectroscopy

The progress of the reaction was carefully monitored using UV/Vis-NIR spectroscopy (Figure 2B) while their spectral changes are very similar. For example, $\mathbf{1}\cdot(ClO_4)_2$ in CH_2Cl_2 exhibited a Soret band at 374 nm, a broad Q-band at 484 nm and a NIR band centred at 890 nm (Figure 2B). However, after addition of trace amount of H_2O to $\mathbf{1}\cdot(ClO_4)_2$, the intensity of the Soret band reduces with a concomitant increase of a new band at 393 nm which eventually decreases again to form a new Soret band at 359 nm along with other bands centred at 470 and 880 nm (Figure 2B) (with a distinct isosbestic point at 380 nm) due to the formation of $\mathbf{2}\cdot(ClO_4)_6$. The most striking feature of the absorption spectrum profile of $\mathbf{2}\cdot(ClO_4)_6$ is the formation of highly intense NIR band (ε, $2.27\times10^5\ M^{-1}cm^{-1}$) at 880 nm owing to the charge resonance phenomena.[9–12] This particular band is due to the π-conjugation across the tetranuclear molecular framework in $\mathbf{2}\cdot(ClO_4)_6$ which is also clearly manifested in the complete alteration of bond lengths at bridging carbons (see below). The spectroscopic features of other intermolecular μ-oxo tetranuclear complexes reported here are grossly alike: the only difference being in the relative positions of their NIR bands which appear at 850, 860 and 875 nm for $\mathbf{2}\cdot(CF_3SO_3)_6$, $\mathbf{2}\cdot(CH_3SO_3)_6$ and $\mathbf{2}\cdot(BF_4)_6$, respectively (Figures 2D and S1).

The UV/Vis-NIR spectrum of $\mathbf{2}\cdot(ClO_4)_6$ was simulated by employing time-dependent density functional theory (TD-DFT) calculations, which corroborates well with the experimental spectrum (Figure 2C). The most significant features of the spectrum are the presence of an intense Q-band at 470 nm and a highly intense NIR band at 880 nm which involve transitions from HOMO to LUMO+4 (oscillator strength, $f\approx0.28$) and HOMO to LUMO ($f\approx0.52$), respectively, with considerable amount of electronic coefficient on the bridging diethyl pyrrole moiety as well as on the central oxygen atom of the μ-oxo motif and thereby confirming the fact that the extensive delocalisation of the π-electron cloud occurs through the pyrrole bridge and also via oxygen atom of the μ-oxo group. The molecular orbitals associated with the main transitions in the TD-DFT calculations are depicted in Figure S2. Remarkably high amplitude of the oscillator strength ($f\approx0.52$) accounts for high intensity of the NIR band as also observed in the experiment.

To investigate the origin of such a high-intense NIR band at 880 nm, a hypothetical analogue of $\mathbf{2}\cdot(ClO_4)_6$ was created by making two –CH= group of the bridge into $-CH_2-$ (Chart S1). In other words, the conjugation was removed, and the entire framework was made non-conjugated. The same TD-DFT calculations were performed on the hypothetical molecule and a very low oscillator strength ($f\approx0.03$) was observed which is almost 18-fold lower in magnitude than the original conjugated molecule (Figure S3). Thus, the high intensity of the NIR band is most likely associated with the long-range electronic communication via conjugated bridge from one end of the molecule to the other end. Afterwards, to check the role of the bridging oxo group, the 'oxo' group was substituted with its congener 'S' to form a hypothetical analogue of $\mathbf{2}\cdot(ClO_4)_6$ with μ-S was modelled (Chart S2), and the TD-DFT calculations were then performed (Figure S4). The calculated spectrum did not match well with the experimentally observed one and the corresponding oscillator strengths are also low compared to that of the original molecule. The observation supports the fact that the delocalisation of electron/charge occurs through the μ-oxo motif also. TD-DFT calculations have also been performed for $\mathbf{2}\cdot(BF_4)_6$ which nicely corroborated with the experimental one (Figure S5). Molecular orbitals associated with the main transitions obtained in the TD-DFT calculations for $\mathbf{2}\cdot(ClO_4)_6$ and $\mathbf{2}\cdot(BF_4)_6$ are demonstrated in Figure S6 while the transitions involving different excited states are summarised in Tables S1 and S2, respectively.

Crystallographic Characterisations

Dark green needle-shaped crystals of $\mathbf{2}\cdot(ClO_4)_6$ and $\mathbf{2}\cdot(BF_4)_6$ were grown via slow diffusion of *n*-hexane into chloroform and dichloromethane solutions of the complexes, respectively, in air at room temperature and the structures were elucidated by X-ray crystallographic analysis. Perspective views of the complexes are depicted in Figure 3 along with the molecular packings in the unit cell are exhibited in Figures S7 and S8. Table S3 lists the crystallographic data and data collection parameters of the complexes reported here, whereas bond lengths and angles are listed in Table S4. Both the molecules crystal-

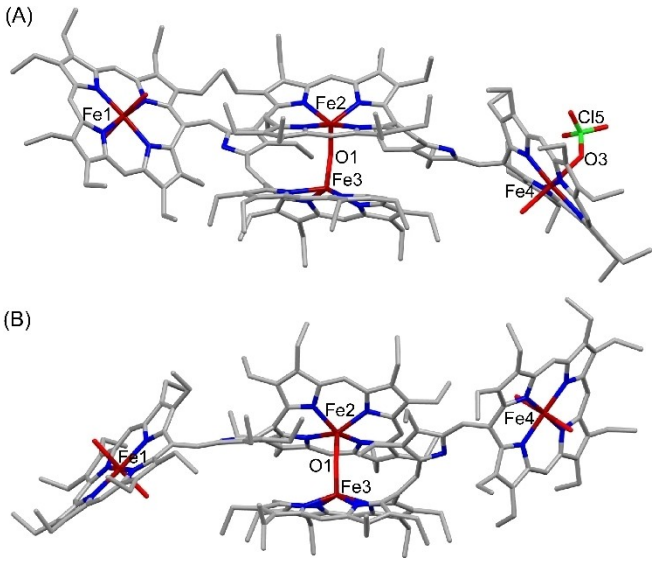

Figure 3. Perspective views (at 100 K) of (A) $\mathbf{2}\cdot(ClO_4)_6$ and (B) $\mathbf{2}\cdot(BF_4)_6$ (H-atoms and counter anions have been omitted for clarity).

lise in triclinic *P*-1 space group. The two terminal iron centres are in six-coordination geometries, one centre with two water molecules and the other centre has one water and one perchlorate as axial ligands in $\mathbf{2}\cdot(ClO_4)_6$, whereas in $\mathbf{2}\cdot(BF_4)_6$ both the iron centres are bound to two water molecules. The two iron centres, which are bound by μ-oxo motif, are five coordinated. The X-ray structures reported here authenticate the formation of the first tetra-cationic tetra-radical intermolecular μ-oxo tetranuclear complexes. Table 1 compares the structural and geometrical parameters of these two complexes.

The molecules are unique in various aspects, as is evident from their different structural and geometrical parametres. The average Fe–N_p distance in $\mathbf{2}\cdot(ClO_4)_6$ are very different: 2.023(8) and 1.998(8) Å, respectively, for cores I and IV, characteristic of admixed intermediate states of iron(III) while 2.084(7) and 2.086(7) Å for cores II and III are indicative of high-spin state.[13–16] Likewise, for $\mathbf{2}\cdot(BF_4)_6$, the average Fe–N_p distances for cores II and III are 2.085(6) and 2.078(6) Å, respectively, which are characteristic of the high-spin state but the same distance is 2.047(6) and 2.017(6) Å for cores I and IV that reflects the admixed intermediate spin state of iron(III).[13–16] The Fe–O bond lengths in the μ-oxo motif are very similar: 1.771(6) and 1.781(6) Å in $\mathbf{2}\cdot(ClO_4)_6$ and 1.789(5) and 1.770(5) Å in $\mathbf{2}\cdot(BF_4)_6$ and are typical Fe–O distance reported for the oxo-bridged dimer. Interestingly, intramolecular μ-oxo dimer of the same pyrrole-bridged porphyrin dimer display Fe–O distances of 1.771(2) and 1.789(2) Å, respectively.[17] The extent of displacements of iron(III) from the mean plane of the $C_{20}N_4$ porphyrinato core (Δ_{24}^{Fe}) are also known to be very characteristic of their spin states in the case of five-coordinate complexes. Such displacements are 0.74 and 0.75 Å, respectively, for cores II and III in $\mathbf{2}\cdot(ClO_4)_6$ which suggests the high spin nature of the iron centres.[13–16]

$\mathbf{2}\cdot(BF_4)_6$ has similar features to that of the $\mathbf{2}\cdot(ClO_4)_6$. The Δ_{24}^{Fe} values for cores II and III are 0.76 and 0.78 Å which bespeak the high-spin state of iron(III).[13–16] The Fe–O–Fe angles are strikingly bent to 145.8(4)° for $\mathbf{2}\cdot(ClO_4)_6$ and 146.9(3)° for $\mathbf{2}\cdot(BF_4)_6$. In contrast, Fe–O–Fe angle reported for the intramolecular μ-oxo dimer of the same pyrrole-bridged porphyrin dimer was 151.97(13)°.[17] In order to minimise the nonbonding interactions between two porphyrin cores connected via oxo-bridge, the porphyrin cores (cores II and III) are significantly twisted with a twist angle of 21.82° and 21.04° for $\mathbf{2}\cdot(ClO_4)_6$ and $\mathbf{2}\cdot(BF_4)_6$, respectively.

The interplanar angle (Θ) between the planes of the bridging pyrrole unit and the porphyrin rings are 35.87°, 43.75°, 45.35° and 38.65° for $\mathbf{2}\cdot(ClO_4)_6$ and 40.69°, 40.34°, 42.3° and 46.65° for $\mathbf{2}\cdot(BF_4)_6$ (Figure S9). Even though the steric interaction with the β-ethyl substituents in the complexes try to obstruct a coplanar disposition of the porphyrin rings and the pyrrole bridge, the substantial conjugation in these complexes impose a higher coplanarity. Extended conjugation among the porphyrin moieties via the diethyl pyrrole bridge moiety is manifested in the alteration of C20–C37, C37–C38, C45–C46, C46–C47, C102–119, C119–C120, C127–C128 and C128–C129 distances which are 1.385(12), 1.449(13), 1.430(13), 1.356(13), 1.396 (12), 1.433 (13), 1.396(12), 1.357(12) Å, respectively (Table S5).

A comparison among the out-of-plane displacement of the porphyrin core atoms have been given in Figure S10. The porphyrin rings are highly distorted in $\mathbf{2}\cdot(ClO_4)_6$ and $\mathbf{2}\cdot(BF_4)_6$ along with the *meso* carbons attached to the bridge which are displaced maximum from the mean plane of the porphyrin ring. As observed from the out-of-plane displacement plots, cores I and IV are more distorted compared to cores II and III for $\mathbf{2}\cdot(ClO_4)_6$ (Figure S10A). Consequently, cores I and IV stabilise the iron(III) in the admixed intermediate spin state whereas cores II and III stabilise the high spin state of iron(III) (see below).

Mössbauer Spectroscopy

To get further insights into the electronic structures, the zero field Mössbauer spectra of three such complexes were

Table 1: Selected structural and geometrical parametres.

Parametres	$\mathbf{2}\cdot(ClO_4)_6$				$\mathbf{2}\cdot(BF_4)_6$			
	Core I	Core II	Core III	Core IV	Core I	Core II	Core III	Core IV
Fe–N_p (Å)[a]	2.023(8)	2.084(7)	2.086(7)	1.998(8)	2.047(6)	2.085(6)	2.078(6)	2.017(6)
Δ_{24}^{Fe} (Å)[b]	0.14	0.74	0.75	0.18	0.11	0.76	0.78	0.10
Δ_{24}(Å)[c]	0.24	0.26	0.25	0.25	0.20	0.27	0.30	0.22
Fe–O1 (Å)	–	1.771(6)	1.781(6)	–	–	1.789(5)	1.770(5)	–
Fe–O(H_2) (Å)	2.087(6)			2.092(6)	2.061(5)			2.125(5)
	2.149(6)				2.063(5)			2.143(6)
Θ (°)[d]	35.87	43.75	45.35	38.65	40.69	40.34	42.38	46.65
Φ (°)[e]	62.67		64.56		68.56		68.39	
Twist angle (°)[f]	–	21.82		–	–	21.04		–
Fe2–O1–Fe3 (°)	145.8(4)				146.9(3)			

[a]Average value. [b] Displacement of iron from the least-squares plane of the $C_{20}N_4$ porphyrinato core. [c] Average displacement of atoms from the least-squares plane of $C_{20}N_4$ porphyrinato core. [d] Inter-planar angle between the least-squares plane of the $C_{20}N_4$ porphyrinato core and the C_4N plane of the bridging pyrrole group. [e] Inter-planar angle between the two least-squares planes of the $C_{20}N_4$ core. [f] Average of the four N–Fe–Fe′–N′ dihedral angles.

recorded at 100 K (Figure 4). In case of $\mathbf{2}\cdot(ClO_4)_6$, two quadrupole-split doublets are clearly visible: one with parametres [$\delta = 0.30$ mm/s, $\Delta E_q = 1.02$ mm/s], suggesting the presence of high-spin iron(III) centre,[13–15] and the other doublet having [$\delta = 0.23$ mm/s, $\Delta E_q = 3.30$ mm/s] is indicative of admixed intermediate spin state[13–15] in the molecule (Figure 4A) as is also evident in the X-ray structure (see above). Figure 4B exhibited two quadrupole-split doublets: [$\delta(\Delta E_q) = 0.34$ (1.56) and 0.27 (3.29) mm/s] corresponding to two non-equivalent Fe(III) centres, one with nearly high spin while the other one being with admixed intermediate spin state in $\mathbf{2}\cdot(CF_3SO_3)_6$. Similarly, trace C shows two quadrupole-split doublets for $\mathbf{2}\cdot(CH_3SO_3)_6$ with parametres: [$\delta(\Delta E_q) = 0.52$ (1.95) and 0.38 (3.41) mm/s] which also indicates two non-equivalent iron(III) centres with similar spin descriptions as observed in $\mathbf{2}\cdot(ClO_4)_6$ and $\mathbf{2}\cdot(CF_3SO_3)_6$.

The X-band EPR spectrum of $\mathbf{2}\cdot(CF_3SO_3)_6$, recorded in CH_2Cl_2-toluene 1:1 mixture at 120 K (Figure S11D), are broad due to overlap of signals which also revealed the presence of two different spin states of iron(III) centres. The simulation of the spectrum yields two set of g values: one being $g_\perp = 5.67$, attributed to the high-spin state of iron whereas the other one with $g_\perp = 4.45$ indicative of the admixed intermediate[13–16] states that are also consistent with the conclusions drawn in the X-ray structure and Mössbauer study (see above) of the complex. The EPR spectra of the other tetranuclear complexes were also similar but very broad (Figure S11A–C). To shed more light on the complex EPR spectra recorded, we have also analysed contributions arising from various excited states based on the J value estimated at 120 K using PHI software (Figure S12). It suggests that multiple spin-states are populated, leading to a broad EPR signal being observed. Also, the Fe-metal centres of core I/IV are expected to have large zero-field splitting (ZFS, $D = -9.35\ cm^{-1}$, from NEVPT2; see ESI).

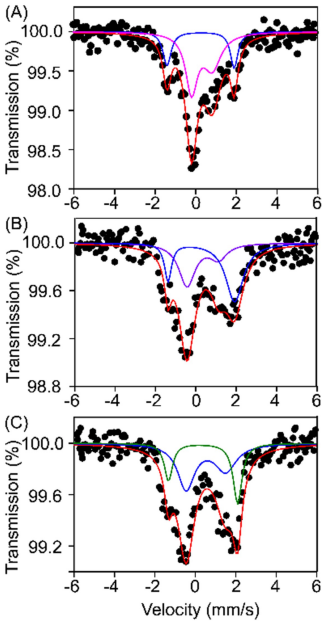

Figure 4. Zero-field Mössbauer spectra of (A) $\mathbf{2}\cdot(ClO_4)_6$, (B) $\mathbf{2}\cdot(CF_3SO_3)_6$ and (C) $\mathbf{2}\cdot(CH_3SO_3)_6$ recorded at 100 K.

^{1}H NMR Spectroscopy

Figure 5 shows a comparison of the ^{1}H NMR spectra of dichlorodiiron(III) pyrrole-bridged porphyrin dimer (**1**) and $\mathbf{2}\cdot(BF_4)_6$. The spectrum of **1** displays sixteen methylene proton resonances between 33.0 to 52.0 ppm, four upfield shifted *meso* signals at $\delta = -7.4$, -54.7, -60.1 and -75.2 ppm and two highly downfield shifted bridging signals at $\delta = 115.9$ and 130.2 ppm (Figure 5A).[9] However, the remarkable features of the ^{1}H NMR spectra of $\mathbf{1}\cdot(BF_4)_2$ are the methylene resonances appearing over a wide range between $\delta = 18.0$ and 63.0 ppm and *meso* proton signals which are largely shifted to the downfield region at $\delta = 20.7$, 25.4, 36.7 and 37.9 ppm due to the presence of porphyrin π-cation radicals.[13,16] Also, bridging protons are located at $\delta = 71.8$ and 81.5 ppm which are very broad because of the extensive conjugation of the radical via the bridge (Figure S13).

The ^{1}H NMR spectrum of $\mathbf{2}\cdot(BF_4)_6$ is similar to $\mathbf{1}\cdot(BF_4)_2$ in the sense that it also exhibits sixteen methylene proton resonances located over a wide range, between $\delta = 20.0$ to 61.2 ppm although the four downfield shifted *meso* signals are poorly resolved for the two terminal porphyrinato cores (cores I and IV). The bridging protons are found at $\delta = 62.9$ and 84.6 ppm which are very broad due to the considerable delocalisation of radicals through the bridging groups as is also evident from the alteration of the bonds (see above). Mulliken spin density calculations for $\mathbf{2}\cdot(ClO_4)_6$ revealed negative spin density residing on the *meso* carbon atoms (Figure S14) and consequently the corresponding proton signals are shifted to the downfield region. However, for the two central porphyrinato cores (cores II and III), it exhibits highly upfield shifted methylene proton resonances ranging from $\delta = 2.0$ to 7.8 ppm. This upfield shift is due to the fact

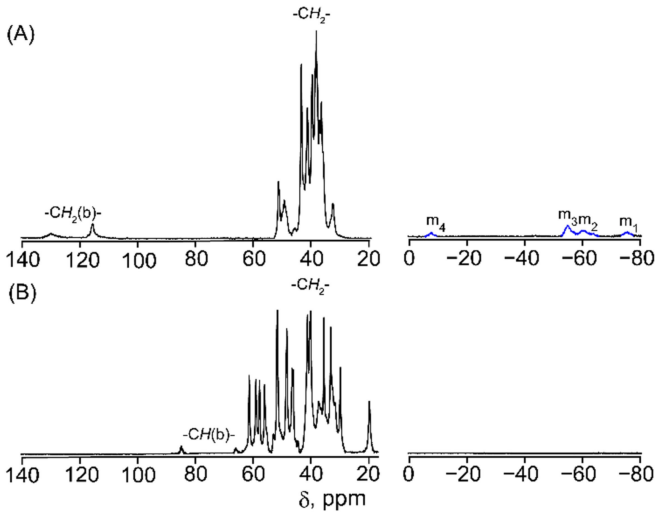

Figure 5. ^{1}H NMR spectra (in $CDCl_3$ at 298 K) of (A) **1** and (B) $\mathbf{2}\cdot(BF_4)_6$. The peaks marked m_1-m_4 denote the *meso* signals.

that two central porphyrinato cores are engaged in a very strong antiferromagnetic coupling mediated through the oxo group.[17] The four *meso* signals were very broad and two bridging protons could be located at 10.9 and 12.9 ppm. The spectral features are very similar for other tetranuclear derivatives (Figure S15).

The proton signals of the tetranuclear complexes are temperature dependent and follows the Curie law (Figure S16) suggesting the existence of a single spin state for each Fe atom throughout the temperature range.

Estimation of Exchange Coupling Constant Using Combined Theoretical and Magnetic Susceptibility Studies

The magnetic susceptibility measurements for $\mathbf{2}\cdot(CF_3SO_3)_6$, $\mathbf{2}\cdot(BF_4)_6$, and $\mathbf{2}\cdot(ClO_4)_6$ were performed at an applied magnetic field of 0.02 T and 0.3 T in the temperature range of 2–30 K and 2–300 K, respectively. Temperature dependent magnetisation for all complexes is shown in Figures 6A and 6B and Figure S17 between 0–300 K. At room temperature, the $\chi_M T$ values of $\mathbf{2}\cdot(CF_3SO_3)_6$, $\mathbf{2}\cdot(BF_4)_6$, and $\mathbf{2}\cdot(ClO_4)_6$ are, respectively, 6.1, 5.5, and 10.7 $cm^3 K mol^{-1}$ and these values differ significantly from the theoretical value of around 14.0 $cm^3 K mol^{-1}$ expected based on uncoupled system (two high-spin Fe(III), two intermediate spin Fe(III) and four radicals). This is due to the presence of strong antiferromagnetic coupling that persists even at room temperature. As the temperature decreases, the $\chi_M T$ decreases gradually till 50 K and then decreases sharply, suggesting various competing exchanges that are operational in these complexes. The susceptibility data indicate dominant antiferromagnetic coupling in all three complexes as the room temperature susceptibility is less than expected for two $S=3/2$ Fe(III), two $S=5/2$ Fe(III) and four radical centres. As there are several exchange coupling constants, fitting the susceptibility data is challenging. Based on the previous reports on dinuclear Fe(III)-radical systems, we have reduced the number of exchange coupling constants to four i.e. J_1 to J_4. The corresponding exchange Hamiltonian is given below.

$$\widehat{H} = -2[J_1(S_{Fe1}S_{Fe1_{rad}} + S_{Fe4}S_{Fe4_{rad}}) + J_2(S_{Fe2}S_{Fe2_{rad}} + S_{Fe3}S_{Fe3_{rad}}) + J_3(S_{Fe2}S_{Fe3}) + J_4(S_{Fe2_{rad}}S_{Fe3_{rad}})]$$

As fitting the susceptibility with four different exchanges can also lead to an over parametrisation problem, we have performed broken symmetry DFT[18] calculations in *Gaussian* suite[19] using UB3LYP/TZVP[20–22] set-up (see computational details for more information) for $\mathbf{2}\cdot(BF_4)_6$, which has a proven track record of yielding good numerical estimates of J values.[22,23] The J_1 interaction describes the exchange coupling between Fe^{III} ($S=3/2$) and the radical ($S=1/2$) present in the same porphyrin system ($Fe1-Fe1_{rad}/Fe4-Fe4_{rad}$). To estimate this interaction, DFT calculations were performed on the model complex (Figure S18). The computed results indicate antiferromagnetic exchange between the $Fe1$ and $Fe1_{rad}$ (similar for $Fe4-Fe4_{rad}$) with the J_1 value of $-11.73\ cm^{-1}$. The unpaired electron in Fe(III) ($S=3/2$) was found to be present in the $(d_{xz})^2(d_{yz})^1(d_{xy})^1(d_{z^2})^1(d_{x^2-y^2})$ orbital having strong overlap with the π-orbital of cationic-porphyrin radical as revealed by the overlap integral (Figure S18C and Table S6), justifying the antiferromagnetic coupling. The interaction is not strong as the overlap is weaker. However, we would like to note here that earlier studies on Fe(III)-radical using several methodologies were found to overestimate the value compared to the experiment.[23] Similarly, the J_2 interaction is the exchange between $Fe2$ and $Fe2_{rad}$ (same between $Fe3$ and $Fe3_{rad}$). To compute the exchange interactions J_1–J_4, we have used a model complex (see Figure S19). The J_2 exchange was computed to be $-27.00\ cm^{-1}$. This interaction is stronger than the J_1 as Fe(III) ($S=5/2$) with five unpaired electrons in the *d*-orbitals open up many strong overlaps that contribute to the antiferromagnetic part of the exchange (Table S7). The J_3 interaction is the exchange coupling between the Fe2 ($S=5/2$) and Fe3 ($S=5/2$) metal centre bridged by $-O^{2-}-$ group, and it is estimated to be $-113.8\ cm^{-1}$. This is consistent with the magneto-structural correlation established already by Boca and co-workers, which suggests that the interaction is strongly correlated with the Fe–O–Fe angle and Fe–O distance.[24a] Here, the Fe–O distance and Fe–O–Fe angle are, respectively, 1.77 Å and 146° and it has been proven that for these distances and angles, exchange interaction will be around $-125\ cm^{-1}$, and the J_3 is in agreement. The strong interaction J_3 among all exchanges is due to the very strong overlap between the *d*-orbitals of (with $d_z^2|p_z|d_z^2$ being the most prominent) Fe metal centres through $-O^{2-}-$ $p_z/p_x/p_y$ orbital (Figure S19C and Table S8). The fourth exchange J_4 is considered the interaction between the core II and core III porphyrin π-cation radicals ($S=1/2$ and $S=1/2$). The radical-radical exchange J_4 was estimated to be $-27.79\ cm^{-1}$. The strong

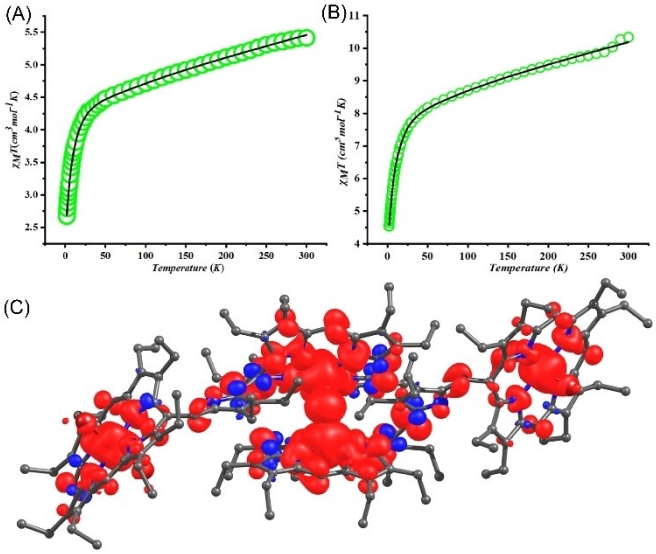

Figure 6. Plot of dc magnetic susceptibility ($\chi_M T$) vs temperature (T) for (A) $\mathbf{2}\cdot(BF_4)_6$ and (B) $\mathbf{2}\cdot(ClO_4)_6$. The black line represents the simulation from the PHI suite.[25] (C) Spin density plot of $[\mathbf{2}]^{6+}$.

Table 2: Simulated and computed exchange-coupling constants in $\mathbf{2}\cdot(X)_6$ with different counter anions.

Exchange type	Spin centres	J_{sim} (cm^{-1}) $\mathbf{2}\cdot(ClO_4)_6$	J_{sim} (cm^{-1}) $\mathbf{2}\cdot(CF_3SO_3)_6$	J_{sim} (cm^{-1}) $\mathbf{2}\cdot(BF_4)_6$	J_{DFT} (cm^{-1}) $\mathbf{2}\cdot(BF_4)_6$
J_1	$Fe1-Fe1_{rad}/Fe4-Fe4_{rad}$	−2.18	−1.60	−1.17	−11.73
J_2	$Fe2-Fe2_{rad}/Fe3-Fe3_{rad}$	−9.17	−4.02	−7.95	−27.00
J_3	$Fe2-Fe3$	−89.85	−68.00	−95.22	−113.8
J_4	$Fe2_{rad}-Fe3_{rad}$	−1.10	−3.61	−0.94	−27.79

exchange here is due to the indirect overlap between the π-orbitals of cationic-porphyrin radicals through the p_x/p_y orbital of the bridging oxygen atoms. Compared to other intra-ion metal radical exchanges, this inter-ion radical-radical exchange was found to be stronger due to the stronger overlap (Table S9). The magnetic exchange values computed by DFT for metal-radical and radical-radical interactions are consistently overestimated, regardless of the functional employed, as previously reported.[24b,c] This is partially due to the fact that calculations were performed only on model complexes instead of the full tetrameric systems and this has been witnessed earlier in polynuclear Fe cages (see ESI for further discussion).[24c]

Magnetic exchange coupling (J_1-J_4) obtained from the DFT has been used as an initial guess to simulate the susceptibility curve (χT *vs.* T simulation) for all the three complexes, $\mathbf{2}\cdot(CF_3SO_3)_6$, $\mathbf{2}\cdot(BF_4)_6$, and $\mathbf{2}\cdot(ClO_4)_6$, using PHI software.[25] The best fit obtained from the simulation has been given in Figure 6, and the magnetic exchange obtained is listed in Table 2. The fitting suggests that, in general, coupling between the unpaired spins of Fe(III) and porphyrin π-cation radical and radical-radical coupling are overestimated by DFT, and it's consistent with our previously reported systems.[23] The Fe($S=5/2$)–Fe($S=5/2$) coupling, J_3 obtained from the simulation is in close agreement with the results obtained from DFT and is found to be stronger for the $\mathbf{2}\cdot(BF_4)_6$ with a simulated value of $-95.22\ cm^{-1}$. A similar value was obtained for the complex $\mathbf{2}\cdot(ClO_4)_6$ having J_3 of $89.85\ cm^{-1}$. However, the J_3 value of $\mathbf{2}\cdot(CF_3SO_3)_6$ is found to be relatively weaker, having a value of $-68.00\ cm^{-1}$. Similarly, the magnetic-exchange coupling J_1, J_2 were found to be stronger for $\mathbf{2}\cdot(ClO_4)_6$ (−2.18 and $-9.17\ cm^{-1}$), followed by $\mathbf{2}\cdot(BF_4)_6$ (−1.17 and $-7.95\ cm^{-1}$) and $\mathbf{2}\cdot(CF_3SO_3)_6$ (−1.60 and $-4.02\ cm^{-1}$) respectively. Moreover, J_4 was found to be stronger for $\mathbf{2}\cdot(CF_3SO_3)_6$ ($-3.61\ cm^{-1}$) followed by $\mathbf{2}\cdot(ClO_4)_6$ ($-1.10\ cm^{-1}$) and $\mathbf{2}\cdot(BF_4)_6$ ($-0.94\ cm^{-1}$). The spin density plot (Figure 6C) suggests that there is strong spin delocalisation throughout the systems via porphyrin π-cation radical. Also, a significant spin density is noted on the bridging oxo oxygen atom due to the spin delocalisation from Fe to O atom. Such a strong delocalisation of spin density across the tetranuclear unit coupled with strong magnetic exchange indicates the nature of orbital overlap among the SOMOs, which suggests that the geometry and the nature of the Fe(III) centres are primarily responsible for the long-range electron/charge transfer observed in the NIR region. The band-observed in the NIR region reveals the transition between one-dimeric unit to the other dimeric unit separated simply by the μ-oxo bridge. A strong antiferromagnetic exchange resulting from the overlap of the d_z^2 orbitals of the Fe(III) centres via the bent μ-oxo moiety hints at the importance of such long-range transfer. The CASSCF/NEVPT2 (complete-active-space self-consistent field/n-electron valence second-order perturbation theory) calculations on model complex **3** and **4** (see Figures S18 and S19) reveal that the core I/IV, Fe metal centre has $S=3/2$ ground state with $S=5/2$ at $133\ kJ\,mol^{-1}$ higher in energy while core II/III Fe metal centre has $S=5/2$ ground state with $S=3/2$ at $266\ kJ\,mol^{-1}$ higher in energy. These observations further support the experimental findings.

Conclusion

In the present study, starting from the dication diradical species of dichlorodiiron(III) porphyrin dimers $\mathbf{1}\cdot(X)_2$ ($X=ClO_4^-$, $CF_3SO_3^-$, $CH_3SO_3^-$ and BF_4^-), a series of π-conjugated tetra-cationic tetra-radical intermolecular μ-oxo tetranuclear complex $\mathbf{2}\cdot(X)_6$ have been synthesised and spectroscopically characterised along with single crystal X-ray structure determination of two such molecules. These species facilitate long-range charge/radical delocalisation through the bridge across the tetranuclear unit, which displays a highly intense NIR band. While iron centres in cores I and IV stabilise in the admixed intermediate spin state, cores II and III stabilise the high spin state of iron(III). Magnetic investigation indicated strong antiferromagnetic coupling between Fe2 and Fe3 through the oxo-bridge, while the interactions between unpaired iron spins and porphyrin π cation radicals are much smaller. Considering the numerous exchange coupling present, DFT calculations were performed and used as a guidance to fit the experimental susceptibility data and offer confidence in the magnetic coupling derived. The identification of an unprecedented near-infrared (NIR) band is linked to robust magnetic exchange, stemming from advantageous orbital overlaps facilitated by the bent μ-oxo moiety.

Acknowledgements

We would like to thank the Science and Engineering Research Board (SERB), India, SERB-STAR (India) and CSIR, New Delhi, for financial support. GR would like to thank SERB (SB/SJF/2019-20/12; CRG/2022/001697) for funding. ECS acknowledges the financial support from the

Spanish Government, (Grant PGC2018-098630-B-I00 and PID2022-137764OB-I00).

Conflict of Interest

The authors declare no competing financial interests.

Data Availability Statement

The data that support the findings of this study are available in the supplementary material of this article. CCDC 2330273 for $\mathbf{2}\cdot(ClO_4)_6$ and 2330274 for $\mathbf{2}\cdot(BF_4)_6$ contain the supplementary crystallographic data for this paper. These data can be obtained free of charge from the Cambridge Crystallographic Data Center via www.ccdc.cam.ac.uk/data_request/cif.

Keywords: Intermolecular μ-oxo tetranuclear complex · tetra-cation tetra-radical · charge-resonance · structure elucidation · DFT study

[1] a) J. Liu, S. Chakraborty, P. Hosseinzadeh, Y. Yu, S. Tian, I. Petrik, A. Bhagi, Y. Lu, *Chem. Rev.* **2014**, *114*, 4366; b) C. M. Paquete, R. O. Louro, *Acc. Chem. Res.* **2014**, *47*, 56; c) H. C. Watanabe, Y. Yamashita, H. Ishikita, *Proc. Natl. Acad. Sci. USA* **2017**, *114*, 2916; d) M. Breuer, K. M. Rosso, J. Blumberger, *Proc. Natl. Acad. Sci. USA* **2014**, *111*, 611; e) D. Leys, T. E. Meyer, A. S. Tsapin, K. H. Nealson, M. A. Cusanovich, J. J. V. Beeumen, *J. Biol. Chem.* **2002**, *277*, 35703.

[2] a) J. Rosenthal, D. G. Nocera, *Acc. Chem. Res.* **2007**, *40*, 543; b) P. D. Harvey, C. Stern, C. P. Gros, R. Guilard, *Coord. Chem. Rev.* **2007**, *251*, 401; c) V. Valderrey, G. Aragay, P. Ballester, *Coord. Chem. Rev.* **2014**, *258*, 137.

[3] a) S. Hiroto, Y. Miyake, H. Shinokubo, *Chem. Rev.* **2017**, *117*, 2910; b) K. Gao, N. Fukui, S. I. Jung, H. Yorimitsu, D. Kim, A. Osuka, *Angew. Chem. Int. Ed.* **2016**, *55*, 13038; c) T. Tamaki, T. Nosaka, T. Ogawa, *J. Org. Chem.* **2014**, *79*, 11029; d) A. A. Ryan, M. O. Senge, *Eur. J. Org. Chem.* **2013**, 3700; e) J. Yang, M.-C. Yoon, H. Yoo, P. Kim, D. Kim, *Chem. Soc. Rev.* **2012**, *41*, 4808; f) J. S. Lindsey, D. F. Bocian, *Acc. Chem. Res.* **2011**, *44*, 638; g) D. Gust, T. A. Moore, A. L. Moore, *Acc. Chem. Res.* **2009**, *42*, 1890.

[4] a) L. Moreira, J. Calbo, J. Aragó, B. M. Illescas, I. Nierengarten, B. Delavaux-Nicot, E. Ortí, N. Martín, J.-F. Nierengarten, *J. Am. Chem. Soc.* **2016**, *138*, 15359; b) S. Ito, S. Hiroto, S. Lee, M. Son, I. Hisaki, T. Yoshida, D. Kim, N. Kobayashi, H. Shinokubo, *J. Am. Chem. Soc.* **2015**, *137*, 142; c) W. Zeng, M. Ishida, S. Lee, Y. M. Sung, Z. Zeng, Y. Ni, C. Chi, D. Kim, J. Wu, *Chem. Eur. J.* **2013**, *19*, 16814.

[5] a) V. S.-Y. Lin, S. G. DiMagno, M. J. Therien, *Science* **1994**, *264*, 1105; b) A. Takai, C. P. Gros, J.-M. Barbe, R. Guilard, S. Fukuzumi, *Chem. Eur. J.* **2009**, *15*, 3110; c) T. E. Clement, D. J. Nurco, K. M. Smith, *Inorg. Chem.* **1998**, *37*, 1150; d) W. J. Cho, Y. Cho, S. K. Min, W. Y. Kim, K. S. Kim, *J. Am. Chem. Soc.* **2011**, *133*, 9364; e) R. Wang, A. M. Brugh, J. Rawson, M. J. Therien, M. D. E. Forbes, *J. Am. Chem. Soc.* **2017**, *139*, 9759; f) M. D. Peeks, C. E. Tait, P. Neuhaus, G. M. Fischer, M. Hoffmann, R. Haver, A. Cnossen, J. R. Harmer, C. R. Timmel, H. L. Anderson, *J. Am. Chem. Soc.* **2017**, *139*, 10461.

[6] a) S. Sarkar, F. S. T. Khan, T. Guchhait, S. P. Rath, *Coord. Chem. Rev.* **2023**, *479*, 215003; b) D. Lai, F. S. T. Khan, S. P. Rath, *Dalton Trans.* **2018**, *47*, 14388; c) T. Guchhait, S. Sasmal, F. S. T. Khan, S. P. Rath, *Coord. Chem. Rev.* **2017**, *337*, 112.

[7] a) F. S. T. Khan, D. Samanta, D. Chandel, S. J. Shah, S. P. Rath, *Inorg. Chem.* **2021**, *60*, 12870; b) F. S. T. Khan, S. J. Shah, S. Bhowmik, F. G. C. Reinhard, M. A. Sainna, S. P. de Visser, S. P. Rath, *Dalton Trans.* **2019**, *48*, 6353; c) S. K. Ghosh, S. P. Rath, *J. Am. Chem. Soc.* **2010**, *132*, 17983.

[8] a) S. Dey, D. Sil, S. P. Rath, *Angew. Chem. Int. Ed.* **2016**, *55*, 996; b) D. Sil, S. Dey, A. Kumar, S. Bhowmik, S. P. Rath, *Chem. Sci.* **2016**, *7*,1212; c) A. K. Singh, M. Usman, S. Sarkar, G. Sciortino, D. Kumar, E. Garribba, S. P. Rath, *Inorg. Chem.* **2021**, *60*, 16492.

[9] a) T. Guchhait, S. Sarkar, Y. A. Pandit, S. P. Rath, *Chem. Eur. J.* **2017**, *23*, 10270; b) S. Sarkar, P. Sarkar, D. Samanta, S. K. Pati, S. P. Rath, *ACS Catal.* **2022**, *12*, 9589.

[10] J. Geng, I. Davis, A. Liu, *Angew. Chem. Int. Ed.* **2015**, *54*, 3692.

[11] a) D. L. Sun, S. V. Rosokha, S. V. Lindeman, J. K. Kochi, *J. Am. Chem. Soc.* **2003**, *125*, 15950; b) A. Takai, M. Chkounda, A. Eggenspiller, C. P. Gros, M. Lachkar, J.-M. Barbe, S. Fukuzumi, *J. Am. Chem. Soc.* **2010**, *132*, 4477; c) Z. Cong, T. Kurahashi, H. Fujii, *Angew. Chem. Int. Ed.* **2011**, *50*, 9935.

[12] a) M. Li, T. J. Neal, G. R. A. Wyllie, A. G. Oliver, C. E. Schulz, W. R. Scheidt, *Inorg. Chem.* **2011**, *50*, 9114; b) K. E. Brancato-Buentello, S.-J. Kang, W. R. Scheidt, *J. Am. Chem. Soc.* **1997**, *119*, 2839.

[13] a) D. Sahoo, M. G. Quesne, S. P. de Visser, S. P. Rath, *Angew. Chem. Int. Ed.* **2015**, *54*, 4796; b) S. Bhowmik, S. K. Ghosh, S. P. Rath, *Chem. Commun.* **2011**, *47*, 4790.

[14] a) R. Weiss, A. Gold, J. Terner, *Chem. Rev.* **2006**, *106*, 2550; b) Y. Ling, Y. Zhang, *J. Am. Chem. Soc.* **2009**, *131*, 6386; c) C.-C. Chen, P. P.-Y. Chen, *Angew. Chem. Int. Ed.* **2012**, *51*, 9325; d) D. Sakow, D. Baabe, B. Bçker, O. Burghaus, M. Funk, C. Kleeberg, D. Menzel, C. Pietzonka, M. Brçring, *Chem. Eur. J.* **2014**, *20*, 2913.

[15] a) W. R. Scheidt, K. M. Kadish, K. M. Smith, R. Guilard (Eds.), *The Porphyrin Handbook*, vol. 3, Academic Press, New York **2000**, pp. 49; b) W. R. Scheidt, C. A. Reed, *Chem. Rev.* **1981**, *81*, 543.

[16] a) F. A. Walker, in *Handbook of Porphyrin Science*, eds.; K. M. Kadish, K. M. Smith, R. Guilard, World Scientific, Singapore **2010**, vol. 6; pp. 1; b) A. Ikezaki, Y. Ohgo, M. Nakamura, *Coord. Chem. Rev.* **2009**, *253*, 2056; c) M. Nakamura, *Coord. Chem. Rev.* **2006**, *250*, 2271; d) S. P. Rath, M. M. Olmstead, A. L. Balch, *J. Am. Chem. Soc.* **2004**, *126*, 6379; e) H. Kalish, J. E. Camp, M. Stépień, L. Latos-Grażyński, M. M. Olmstead, A. L. Balch, *Inorg. Chem.* **2002**, *41*, 989.

[17] D. Sil, F. S. T. Khan, S. P. Rath, *Chem. Eur. J.* **2016**, *22*, 14585.

[18] W. Kohn, A. D. Becke, R. G. Parr, *J. Phys. Chem.* **1996**, *100*, 12974.

[19] A. Frisch, *Wallingford, USA.* **2009**, *470*, 25p.

[20] M. F. Peintinger, D. V. Oliveira, T. Bredow, *J. Comput. Chem.* **2013**, *34*, 451.

[21] J. Tirado-Rives, W. L. Jorgensen, *J. Chem. Theory Comput.* **2008**, *4*, 297.

[22] N. Berg, T. N. Hooper, J. Liu, C. C. Beedle, S. K. Singh, G. Rajaraman, S. Piligkos, S. Hill, E. K. Brechin, L. F. Jones, *Dalton Trans.* **2013**, *42*, 207.

[23] S. K. Singh, G. Rajaraman, *Chem. Eur. J.* **2014**, *20*, 113.

[24] a) B. Vranovičová, R. Boča, *Nova biotechnologica et Chimica* **2013**, *12*, 70; b) M. Atanasov, P. Comba, S. Hausberga, B. Martin, *Coord. Chem. Rev.* **2009**, *253*, 2306; c) A. E. Dearle, D. J. Cutler, H. W. L. Fraser, S. Sanz, E. Lee, S. Dey, I. F. Diaz-Ortega, G. S. Nichol, H. Nojiri, M. Evangelisti, G.

Rajaraman, J. Schnack, L. Cronin, E. K. Brechin, *Angew. Chem. Int. Ed.* **2019**, *58*, 16903.
[25] N. F. Chilton, R. P. Anderson, L. D. Turner, A. Soncini, K. S. Murray, *J. Comput. Chem.* **2013**, *34*, 1164.
[26] J. Olsen, *Int. J. Quantum Chem.* **2011**, *111*, 3267.
[27] C. Angeli, R. Cimiraglia, S. Evangelisti, T. Leininger, J.-P. Malrieu, *J. Chem. Phys.* **2001**, *114*, 10252.
[28] F. Neese, *Wiley Interdisciplinary Reviews: Computational Molecular Science* **2018**, *8*, e1327.

Manuscript received: February 1, 2024
Accepted manuscript online: March 13, 2024
Version of record online: April 23, 2024